Numerical Simulation of Shock Wave Reflecting Patterns for Different Flow Conditions

Sung-Yoon Choi* and Sejong Oh**

Department of Aerospace Engineering
Pusan National University, Busan City, Korea 609-735

Abstract

The numerical experiment has been conducted to investigate the unsteady shock wave reflecting phenomena. The cell-vertex finite-volume, Roe's upwind flux difference splitting method with unstructured grid is implemented to solve unsteady Euler equations. The 4th-order Runge-Kutta method is applied for time integration. A linear reconstruction of the flux vector using the least-square method is applied to obtain the 2nd-order accuracy for the spatial derivatives. For a better resolution of the shock wave and slipline, the dynamic grid adaptation technique is adopted. The new concept of grid adaptation technique, which is much simpler than that of conventional techniques, is introduced for the current study. Three error indicators (divergence and curl of velocity, and gradient of density) are used for the grid adaptation procedure. Considering the quality of the solution and the numerical efficiency, the grid adaptation procedure was updated up to 2nd level at every 20 time steps. For the convenience of comparison with other experimental and analytical results, the case of interaction between the straight incoming shock wave and a sharp wedge is simulated for various flow conditions.

The numerical results show good agreement with other experimental and analytical results, in the shock wave reflecting structure, slipline, and the trajectory of the triple points. Some critical cases show disagreement with the analytical results, but these cases also have been proven to show hysteresis phenomena.

Key Word : reflecting shock wave structure, Euler equations, slipline, Roe scheme, unstructured grid, dynamic grid adaptation

Introduction

The shock wave reflecting phenomena occurs when a moving shock wave collides with bodies. The structure of the reflected shock wave configuration shows various patterns depending on the Mach number of the moving shock wave and the body slope angle. Many researchers have investigated the shock wave reflection phenomena with analytic[1], numerical[2,3], and experimental methods[4].

For the analytic study in the case of the interaction of the straight incoming shock wave with the wedge, researchers considered the flow as a pseudo-steady state because of its self-similar characteristics. The shock wave reflecting patterns are categorized as Regular reflection (RR) and Mach reflection(MR). The Mach reflection is subdivided as single-Mach reflection(SMR), transitional-Mach reflection(TMR), and double-Mach reflection(DMR) depending on the patterns of reflecting shock wave and the slipline. SMR was first observed by Mach in 1878, TMR by Smith in 1945, and DMR by White in 1951. Ben-Dor proved analytically that two

---

* Graduate student, currently in KAIST
** Associate Professor
   E-mail : tazo@pusan.ac.kr,   TEL : 051-510-2435,   FAX : 051-513-3760

different DMR patterns are possible depending on the trajectory angle of first and second triple points[1]. Lee and Glass verified this hypothesis experimentally and termed them as the positive/negative double-Mach reflection[1]. Recently, with the aid of high speed computers and the accurate numerical schemes, several researchers have conducted the numerical studies on the shock wave reflecting phenomena, mostly for the cases of complicated internal and external flow fields[4,5,6]. But to resolve the complicate shock wave structures accompanying the slipline, the numerical scheme requires appropriate grid reconstructing techniques. Physically, the slipline is defined as the discontinuity in Mach number, while the pressure is continuous across it. The shock wave and the slipline are known to be caused by the inviscid nature. Numerically and physically, the amount of discontinuity of the shock wave is much stronger than that of the slipline. Therefore, to resolve the slipline numerically with the existence of shock wave, a new concept of grid refinement criteria is required.

In the present study, the numerical experiments have been conducted to resolve the shock wave reflecting phenomena with the concept of dynamic grid adaptation techniques. The flow domain is constructed to simulate the interaction of the straight incoming shock wave with a wedge, which is the same as that of the analytical study. The upwind Roe scheme with 2nd-order of accuracy has been implemented to solve the unsteady Euler equations, since the shock wave and the slipline are inviscid nature. For the time integration, 4th-order Runge-Kutta method is adopted. Three parameters, (divergence of velocity, variation of density, and vorticity), have been chosen as the error indicators for the grid adaptation procedure.

The numerical results obtained from the current study are verified by comparing with other analytical and experimental results.

Governing Equations and Numerical Scheme

1. Governing Equations and Boundary/Initial Conditions

1.1 Governing Equations

The governing equations are the conventional unsteady two-dimensional Euler equations, and the integral form of the equations is expressed as

$$\frac{\partial}{\partial t} \int \int_{\Omega} \boldsymbol{Q} d\Omega + \oint_{s} \boldsymbol{F} \cdot \boldsymbol{n} ds = 0$$

where $\boldsymbol{Q}$ and $\boldsymbol{F}$ is the flow variables and the flux vector respectively.

1.2 Boundary Condition

As can be seen in Fig. 1, which shows the flow domain schematically, the flow tangency condition is applied at the inviscid and reflecting walls. At inlet and outlet boundaries, the conventional subsonic and supersonic conditions are imposed respectively.
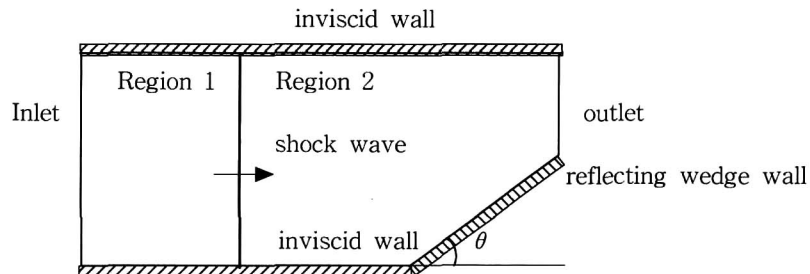

Fig. 1. Schematic flow domain.

1.3 Initial Condition

The initial condition was imposed similar to the shock tube problem. The pressures at region 1 and 2 are given to obtain a desired incident shock wave Mach number. Other variables are given from the shock tube relations[7].

2. Numerical Implementation

2.1 2nd-Order Accuracy Roe Scheme

For numerical calculations, the governing equations are discretized using the cell-vertex FVM. The discrete form of the governing equations about i^{th} cell is

$$\Omega_i \frac{\partial Q}{\partial t} + \sum_{j=k(i)} F_{ij}\, l_{ij} = 0$$

where i is the node number, j is the number of the face of the cell, and F_{ij} is the inviscid flux vector.

The flux vector can be represented using the Roe's flux-difference splitting method as[8,9]

$$F_{i,j} = \frac{1}{2}\left[F(Q_L) + F(Q_R) - |A|(Q_R - Q_L) \right]$$

where Q_L and Q_R are the state variables to the left and right of the interface.

The Roe's flux formula can be reduced to four $\triangle F$ flux components as

$$|A|(Q_R - Q_L) = |\triangle F|_1 + |\triangle F|_2 + |\triangle F|_3 + |\triangle F|_4$$

The 2nd-order of spatial accuracy can be obtained from the Taylor series expansion[10] as

$$Q_i^R = Q_i + \Phi(\nabla Q)_i \cdot r_{ij}, \qquad Q_j^L = Q_j + \Phi(\nabla Q)_j \cdot r_{ji}$$

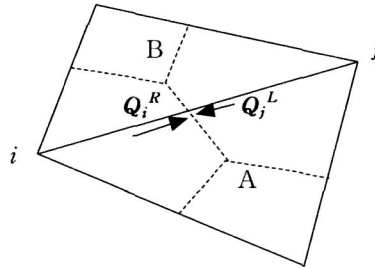where Q_i^R and Q_j^L are the properties of flow variables at the control boundary as shown in Fig. 2.

Fig. 2. Fluxes at control boundaries.

∇Q can be obtained by using the least-square method assuming the properties are continuous between neighbor nodes as

$$Q_i = Q_0 + Q_{x_0}(x_i - x_0) + Q_{y_0}(y_i - y_0)$$

where

$$Q_{x_0} = \sum_{i=1}^{N} W_i^x(Q_i - Q_0), \qquad Q_{y_0} = \sum_{i=1}^{N} W_i^y(Q_i - Q_0)$$

$$W_i^x = \frac{x_i - x_0}{r_{ii}^2} - \frac{r_{12}}{r_{11}r_{22}^2}\left[(y_i - y_0) - (x_i - x_0)\frac{r_{12}}{r_{11}}\right], \qquad W_i^y = \frac{1}{r_{22}^2}\left[(y_i - y_0) - (x_i - x_0)\frac{r_{12}}{r_{11}}\right]$$

and

$$\gamma_{11} = \left[\sum_{i=1}^{N}(x_i-x_0)^2 \right]^{\frac{1}{2}}, \quad \gamma_{12} = \frac{\sum_{i=1}^{N}(x_i-x_0)(y_i-y_0)}{\gamma_{11}}, \quad \gamma_{22} = \left[\sum_{i=1}^{N}\left((y_i-y_0)-(x_i-x_0)\frac{\gamma_{12}}{\gamma_{11}} \right)^2 \right]^{\frac{1}{2}}$$

Here Q_0, x_0, y_0 are the flow variables and the coordinates at the centroid, and Q_i, x_i, y_i are those of neighboring node.

To reduce the oscillation of the solution and to maintain the solution monotony, the flux limiter Φ suggested by Barth[11] is used as

$$Q_i^{min} \leq Q_i \leq Q_i^{max}$$

where

$$Q_i^{min} = min(Q_i , Q_{neighbors}) \qquad Q_i^{max} = max(Q_i , Q_{neighbors})$$

$$\Phi_{ik} = \begin{cases} min\left(1, \dfrac{Q_i^{max} - Q_i}{Q_k - Q_i}\right) & \text{if } Q_k - Q_i > 0 \\[2mm] min\left(1, \dfrac{Q_i^{min} - Q_i}{Q_k - Q_i}\right) & \text{if } Q_k - Q_i < 0 \\[2mm] 1 & \text{if } Q_k - Q_i = 0 \end{cases}$$

2.2 Time Integration

The semi-discrete from of the governing equations is

$$\Omega_i \frac{\partial Q_i}{\partial t} + R_i = 0 , \quad i = 1, 2, 3$$

where R_i is the residual accrued from the fluxes through the faces of the ith cell.

These equations are integrated by using an explicit four-stage Runge-Kutta method[12].

3. Grid Refinement/Coarsening Techniques

3.1 Error indicators

For the grid adaptation (refinement/coarsening) procedure, error indicators are used for the detection of the region with large gradients of flow properties. For the current study, three different error indicators are used to resolve the reflecting shock wave and the slipline.

$$\tau_{d_i} = |\nabla \cdot V| l_i^{\frac{\gamma+1}{\gamma}} , \quad \sigma_d = \sqrt{\frac{\sum_{i=1}^{n}\tau^2_{d_i}}{n}} \qquad : \text{divergence of velocity}$$

$$\nabla \times V, \quad or \quad \frac{\oint_c V \cdot ds}{\text{Area of Cell}} \qquad : \text{vorticity}$$

$$E_i = \frac{|\sum_{j=1}^{i(i)}(\rho_j - \rho_i)|}{\sum_{j=1}^{i(i)}|\rho_i - \rho_j| + \varepsilon \sum_{j=1}^{i(i)}|\rho_j + \rho_i|} \qquad : \text{density gradient}$$

The node points satisfying anyone of the three criteria, are selected for grid refinement/coarsening. The vorticity and the density gradient are used for detecting the shock wave, and the divergence of velocity is for the slipline.

3.2 Grid Adaptation Method

In general, most of the grid adaptation techniques use one of the following methods; grid movement

(r-refinement), grid enrichment (h-refinement), and local solution enhancement (p-refinement). For the h-refinement method, more nodes are added to the regions where higher resolution of the solution is required. The nodes can also be removed from the location where the solution is smooth.

In this study, the h-refinement method is used for the grid adaptation because it is efficient and fast. The "parent" cell in the high gradient region, determined by the error indicators around the shock wave and the slipline location, is subdivided into four "son" cells, and the neighbor of the "parent" cell into two "son" cells[13,14].

Generally, the grid coarsening procedure is the reverse of the refinement process such that the error indicators detect the smooth flow region, and the cells around the region are amalgamated by reducing the number of cells until the requirements are satisfied. Because of the numerical complexity of this coarsening procedure, a new simple grid coarsening concept is introduced in the current study by returning the grid to the initial state. This algorithm is logically simple and numerically fast comparing to the general coarsening method, at the expense of more memory space.

The grid adaptation procedure is shown in Fig. 3. At the beginning of the adaptation procedure, the previous grid pattern returns to its initial state through the following process.

  step 1) Remove all adapted cells which were divided from their "parent" cells in previous grid pattern, while all nodes are retained (Fig. 3b.).
  step 2) Remove added nodes, and all the flow properties, which are stored in removed nodes, are stored in a temporary array with their coordinate information. The grid returns to its initial state as shown in Fig. 3c.
  step 3) New grid refinement is made for the nodes and cells as selected by the error indicators (Fig. 3d.).

The grid adaptation procedure is performed at every 20 iterations for the calculation efficiency, and the adaptation level is selected up to 2nd level, which is enough to resolve the shock wave and the slipline.
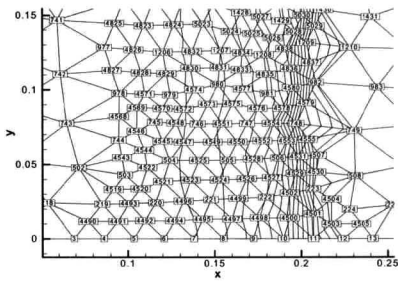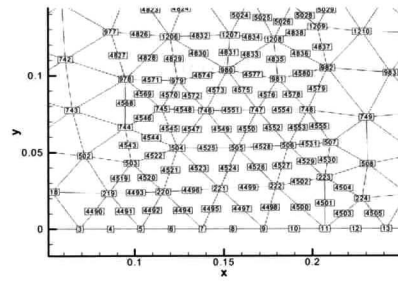

Fig. 3a. Previous grid pattern
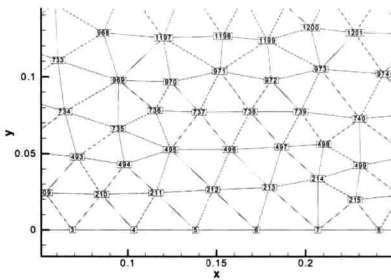

Fig. 3b. Remove added cells
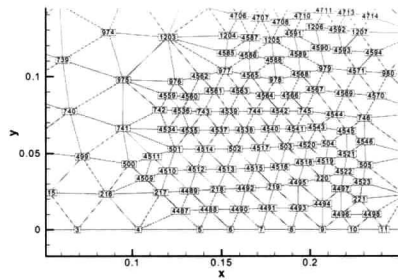

Fig. 3c. Remove added nodes

Fig. 3d. New adaptation grid

Fig. 3. Grid adaptation procedure.

Results and Discussion

1. Grid Adaptation

Figs. 4~6 show the effect of the grid adaptation for the flow conditions of $\theta = 40^{\circ}$ and $M_s = 2.75$. As can be seen from Figs. 4~6, the shock wave and the slipline can be more clearly observed as the adaptation level increases. All the numerical results presented below are the ones with the grid after the 2nd adaptation level.
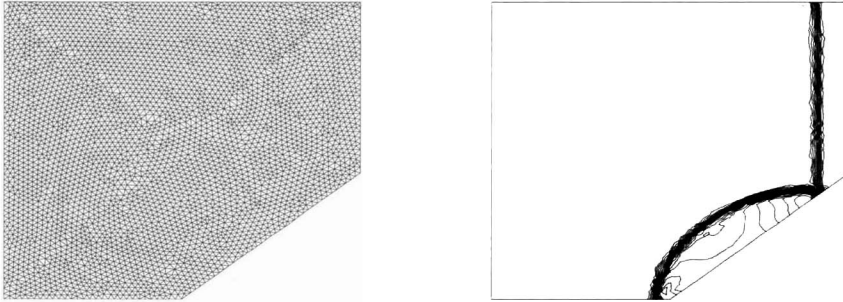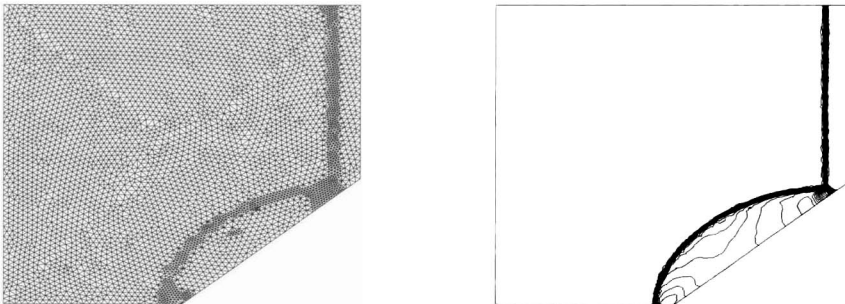

Fig. 4. Initial grid and density contour.

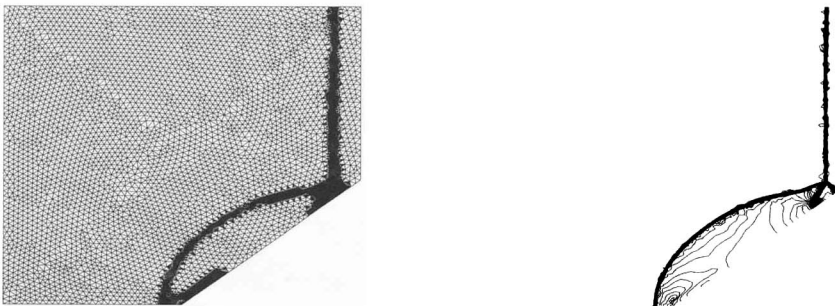Fig. 5. 1st adaptation grid and density contour.

Fig. 6. 2nd adaptation grid and density contour.

2. Regular Reflection (RR)

The schematic shock wave structure is shown in Fig. 7. It shows the incident shock wave(i) and the reflected shock wave(r) emanates from the reflection point(R). Since RR satisfies the sonic criterion, it is attached at the reflection wedge surface.

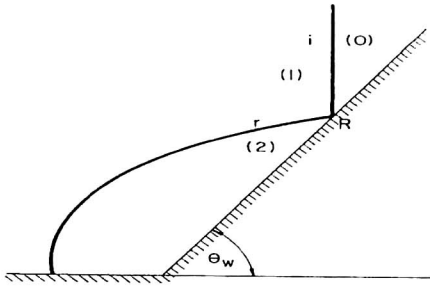Fig. 8 is the holographic interferogram obtained from the experiment at the flow condition
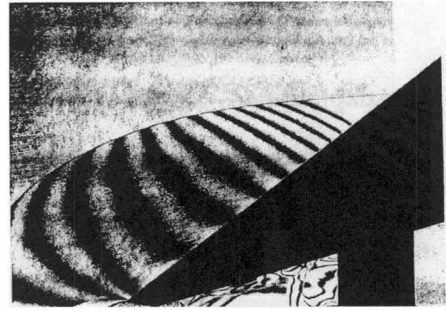
Fig. 7. RR wave configuration.

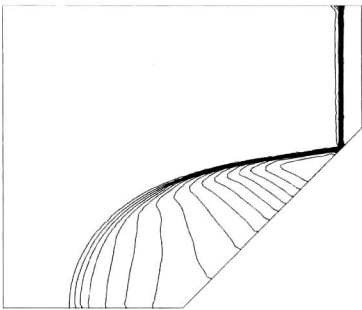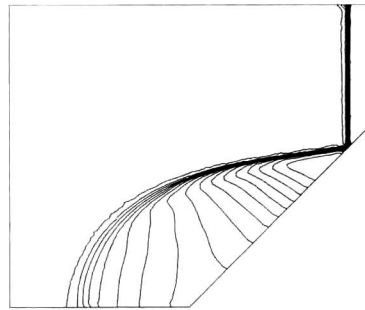Fig. 8. Holographic interferogram.

Fig. 9. Density contour.

Fig. 10. Pressure contour.

of $\theta = 50°$ and $M_s = 1.17$[1]. Figs. 9 and 10 show the numerical results of the density and pressure contours for the same flow condition. The numerical results match well with the experiment.

3. Single-Mach Reflection (SMR)

SMR has four discontinuities (incident shock wave i, reflecting shock wave r, Mach stem m, and slipline s) intersecting at the triple point T as shown in Fig. 11. The triple point is moving along a straight line originating at the leading-edge of the reflecting wedge. The holographic interferogram in Fig. 12 is for the case of a flow condition at $\theta = 35°$ and $M_s = 1.75$[1]. Unlike the incident shock wave, the reflected shock wave, the Mach stem, and the slipline are curved.
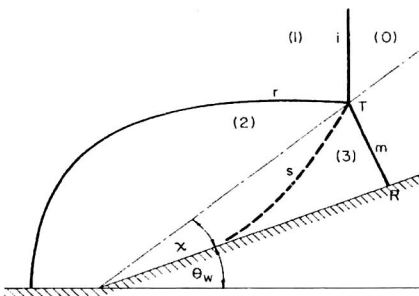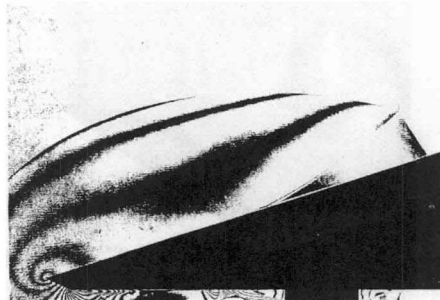

Fig. 11. SMR wave configuration.

Fig. 12. Holographic interferogram.

Figs. 13 and 14 show the numerical results for the same flow condition, and show good agreement with the experiment. As expected, the slipline can be clearly visible in Fig. 13, while the pressure is continuous across the slipline as in Fig. 14. Fig. 15 shows the trajectory of the triple point.
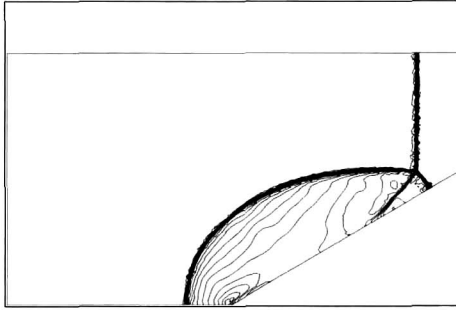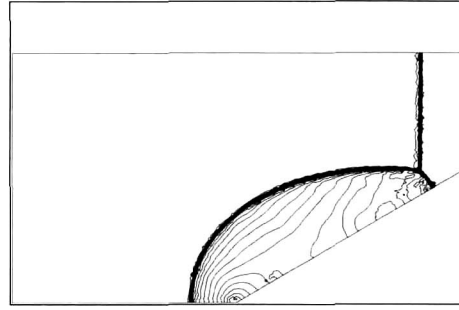
Fig. 13. Density contour.
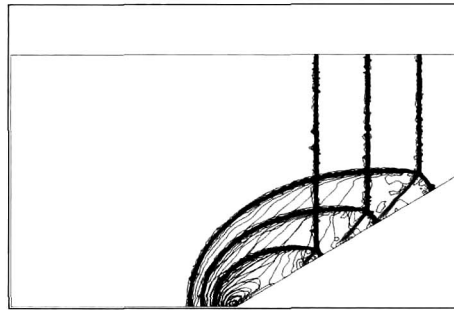

Fig. 14. Pressure contour.

Fig. 15. Trajectory of the triple point.

4. Transitional-Mach Reflection (TMR)

TMR occurs when the flow Mach number behind the reflected shock wave is supersonic with respect to the triple point T. The wave configuration of TMR, as shown in Fig. 16, is similar to that of SMR except the existence of the point known as the kink K. Similar to the triple point, the kink moves along a straight line originating from the leading-edge of the reflecting wedge. For the case of TMR, the slipline is curled forward because of the strong compression wave behind the slipline as shown in Figs. 16 and 17.

Fig. 16. TMR wave configuration.

Fig. 17. Holographic interferogram.

Fig. 17 shows the interferogram for the flow condition of $\theta = 40°$ and $M_s = 2.96$ [1]. The numerical results of the density and pressure contours for the same flow condition are shown in Figs. 18 and 19. In Fig. 20, it is shown that the high pressure region exits immediately behind the curled slipline.

5. Double-Mach Reflection (DMR)

When the flow Mach number behind the kink becomes supersonic, the shock wave configuration

Fig. 18. Density contour.

Fig. 19. Pressure contour.

Fig. 20.   Pressure contour around the slipline.

becomes DMR. For this case, there appear a second triple point T' and another shock wave r'. The second triple point is complemented by a second slipline s'. The schematic diagram for these phenomena is shown in Fig. 21. The interferogram obtained from the experiment is shown in Fig. 22 for the flow condition of $\theta = 47^o$ and $M_s = 2.74$ [1].
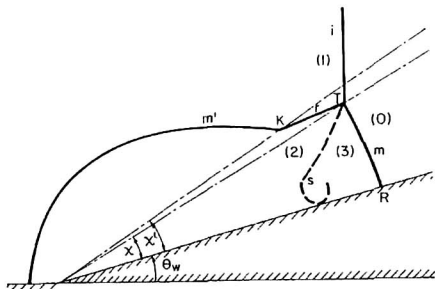

Fig. 21. DMR wave configuration.

Fig. 22. Holographic interferogram.

DMR is subdivided into three categories as positive DMR (DMR$^+$), negative DMR (DMR$^-$), and terminal DMR (TDMR), depending on the relation between the trajectory angles of the first and second triple points, x and x'.

5.1 Positive/Negative DMR (DMR$^+$/DMR$^-$)

As mentioned previously, DMR$^+$ is defined when $x < x'$, while DMR$^-$ is when $x > x'$. These are named by Lee and Glass[1]. DMR$^+$ is the case when the DMR shock wave configuration is the mostly clearly observed in the current numerical study.

Fig. 23. Density contour [DMR⁺].
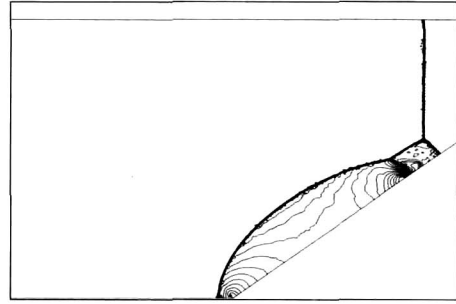
Fig. 24. Pressure contour [DMR⁺].
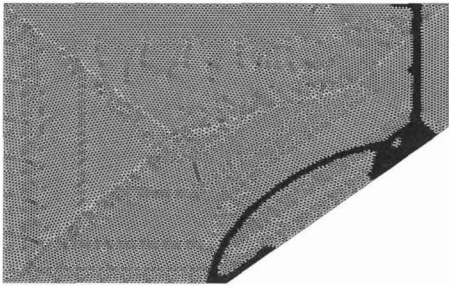
Fig. 25. Grid pattern for DMR⁺.
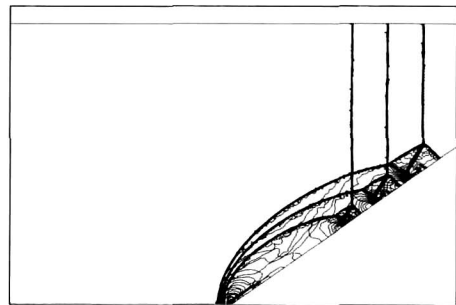
Fig. 26. Trajectories of the two triple points. [DMR⁺]

The numerical results for the case of $\theta = 40^o$ and $M_s = 4$, which is the case of DMR⁺, are shown in Figs. 23 and 24. All of the physical phenomena explained in the previous section can be similarly observed from the results except for the second slipline s'. s' is not observed clearly even from the experiment. However, existence of s' can be expected from the result of the grid pattern shown in Fig. 25, and it is also expected that the discontinuity across s' is very weak. Fig. 26 shows the trajectories of the two triple points.

5.2 Another DMR and TDMR

Another case of DMR is the limiting case between DMR⁺ and DMR⁻, which occurs when $x = x'$, and TDMR is the case when $x' = 0$. The density contours for $x \simeq x'$ are shown in Figs. 27a and 27b for the condition of $\theta = 47^o$ and $M_s = 3.5$, which is the most likely are case of $x = x'$ obtained from the current simulation.

As can be seen from the figure, all discontinuities are confined within a very small region. The results of TDMR cannot obtained by using the current techniques due to the lack of viscosity.
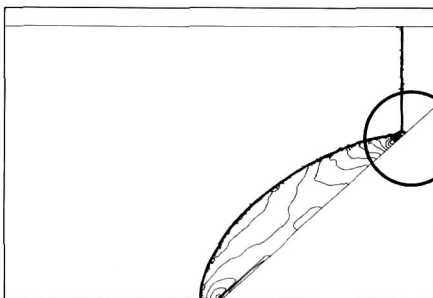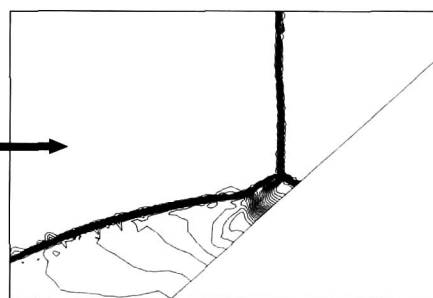

Fig. 27a. Density contour.

Fig. 27b. Enlarged resolution.

6. Overall Comparison with experiment and analytic studies

All of the shock wave reflection patterns for different incident shock wave Mach numbers and wedge angles were also shown in Fig. 28. The lines separating regions are the analytical results, the filled symbols represent experimental results, and the blank symbols are the current numerical results.

There are some discrepancies between the analytical and the experimental, numerical results. But most of the discrepancies are the cases close to the borderline obtained from the analytical result. Ivanov et. al.[6] suggested the hypothesis that a hysteresis phenomen occurs in the transition between RR and MR of strong shock wave, which was first suggested by Hornung[15]. This hypothesis can explain these discrepancies.
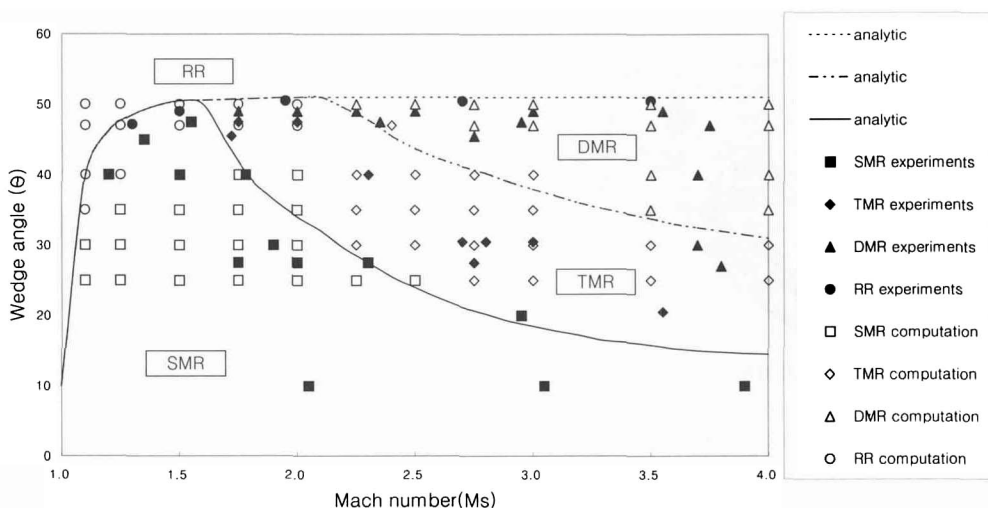

Fig. 28. Comparision of experimental and computational results.

Conclusions

The different shock wave reflection patterns are studied by using a numerical simulation of the unsteady Euler equations and a simple grid adaptation method. The shock wave configuration and the slipline can be resolved with a proper grid distribution. All of the physical phenomena, which cannot be measured from experiment, were observed and explained from the numerical results. Results for some special cases such as DMR and TDMR cannot be obtained since the complicated shock wave and the slipline phenomena appear within a very small region, which require to resolve the Navier-Stokes' equations.

Acknowledgement

References

1. Ben-Dor, Gabi, *Shock Wave Reflection Phenomena*, Springer-Verlag Inc., New York, 1992.
2. Baum, J. D. and Lohner, R., "Numerical Simulation of Shock-Box Interaction Using an Adaptive Finite Element Scheme," *AIAA Journal*, Vol. 32, No. 4, 1994, pp. 682-692.

3. Choi, W. S., "Numerical analysis of steady/unsteady compressible flow fields using finite volume TVD schemes," Ph. D. Thesis, Postech, 1994.

4. Yang, H., "Impingement of a Moving Shock Wave into a Cavity," Master Thesis, KAIST, 1998.

5. Lohner, R. and Baum, J. D., "Numerical Simulation of shock Interaction with Complex Geometry Three-Dimensional Structures Using A New Adaptive H-Refinement Scheme on Unstructured Grids," AIAA paper 90-0700, 1990.

6. Ivanov, M. S., Gimelshein, S. F. and Beylich, A. E., "Hysteresis effect in stationary reflection of shock waves," *Phys. Fluids*, Vol. 7, No. 4, 1995, pp. 685-687.

7. Anderson, J. D., Jr., *Modern Compressible Flow*, McGraw-Hill Publishing Company, 1990.

8. Roe, P. L., "Characteristic Based Schemes for the Euler Equations," *Annual Review of Fluid Mechanics*, Vol. 18, 1986, pp. 337-365.

9. Fink, N. T., "Upwind Scheme for Solving the Euler Equations on Unstructured Tetrahedral Meshes," *AIAA Journal*, Vol. 30, No. 1, 1992, pp. 70-77.

10. Anderson, W. K. and Lhaus, D., "An Implicit Upwind Algorithm Computing Turbulent Flows In Unstructured Grid," *Computers and Fluids*, Vol. 23, No. 1, 1994, pp. 1-21.

11. Barth. T. J. and Jespersen, D. C., "The Design and Application of Upwind Scheme on Unstructured Meshes," AIAA paper 89-0366, 1989.

12. Kozic, M. S. and Sredojevic, D., "Development of unstructured dynamic grids for solving unsteady two-dimensional Euler equations," *The Aeronautical Journal*, Vol. 102, No. 1014, 1998, pp. 195-200.

13. Lohner R., "AN ADAPTIVE FINITE ELEMENT SCHEME FOR TRANSIENT PROBLEMS IN CFD," *Computer Methods in Applied Mechanics and Engineering*, Vol. 61, 1987, pp. 323-338.

14. Pizadeh, S. Z., "An Adaptive Unstructured Grid Method by Grid Subdivision, Local Remeshing, and Grid Movement," AIAA paper 99-3255, 1999.

15. Ivanov, M. S., et. al, "Numerical Analysis of Shock Wave Reflection Transition in Steady Flows," *AIAA Journal*, Vol. 36, No. 11, 1998, pp. 2079~2086.

16. Cho, K. H., "The Optimal shape design using adjoint method on unstructured meshes," Master Thesis, Pusan National University, 2000.

17. Kim, S. H., "Numerical Simulation of Shock_Induced Combustion on Adaptive Unstructured Grid," Master Thesis, Pusan National University, 2001.